JOURNAL OF THEORETICAL
AND APPLIED MECHANICS
https://doi.org/10.15632/jtam-pl/203691
ONLINE FIRST

INVESTIGATION OF FLOW CONTROL ON A VERTICAL AXIS WIND TURBINE USING A BIONIC FLAP

Mingtong ZHOU[1], Junwei ZHONG[1*], Qiqi ZHANG[1], Yufeng GAN[1], Chaolei ZHANG[1], Huizhong LIU[2]

[1] *School of Mechanical and Electrical Engineering, Jiangxi University of Science and Technology, Ganzhou, China*
[2] *Jiangxi Province Engineering Research Center for Mechanical and Electrical of Mining and Metallurgy, Jiangxi University of Science and Technology, Ganzhou, China*

*corresponding author, *jwzhong0@jxust.edu.cn*

Inspired by the slight lift of bird feathers at the trailing edge under specific conditions, an adjustable bionic flap (BF) was added to a vertical-axis wind turbine (VAWT) to improve its aerodynamic performance. Numerical simulations using the SST turbulence model were conducted to examine the BF's flow control mechanism and how its geometry affects the VAWT's power coefficient. The results show that the BF can evidently improve the power coefficients of the VAWT. Compared with the original VAWT, the power coefficient of the VAWT with an adjustable BF is increased by 45.2 % at $\lambda = 1.75$.

Keywords: vertical axis wind turbine; bionic flap; aerodynamic performance; flow control.

1. Introduction

In recent years, the occurrence of severe weather and climate phenomena has been escalating globally, predominantly attributed to the rise in global temperatures. A primary contributor to this global occurrence is the reliance on mineral fuels, which emit significant amounts of greenhouse gases. Transitioning away from mineral fuels presents one of the most significant challenges of the 21st century. Consequently, wind power has garnered significant interest as a prospective substitute (Rehman *et al.*, 2023; McKenna *et al.*, 2025).

Wind turbines are the primary apparatus used to harness wind energy. They can be divided into two principal groups based on the orientation of their rotating shafts: horizontal-axis wind turbines (HAWTs) and vertical-axis wind turbines (VAWTs). VAWTs present significant advantages compared to HAWTs, including omnidirectional operation, improved structural scalability, and enhanced system stability (Abdolahifar & Zanj, 2025). Owing to these advantages, VAWTs are increasingly favored in urban, remote, and offshore settings. Nevertheless, VAWTs are at present defined by their lower energy conversion efficiency in comparison with HAWTs. Several attempts have been made to enhance the aerodynamic performance of VAWTs through various flow control techniques (Zhao *et al.*, 2022; Tayebi & Torabi, 2024). Many researchers highlight the significance of applying these control methods near the blade's leading edge to impact the onset of flow separation. The vortex generator (VG) is a simple apparatus made up of several mini plates, usually mounted on the suction surface of a blade airfoil near the leading edge. While the mechanisms of VGs on airfoils and HAWTs have been extensively studied, relatively less research has focused on their application in VAWTs. Yan *et al.* (2019) proposed the use of micro VGs with heights less than half of the boundary layer thickness for VAWTs. Flow separation on a VAWT blade tends to happen alternatively on the suction and pressure surfaces. A VG with excessive height can generate additional drag, which may undermine its aerodynamic advantages. Zhong *et al.* (2019) proposed an innovative approach by replacing conventional VGs with an elevated rod positioned in front of the blade's leading edge. Ullah *et al.* (2020) used leading-edge slats to reduce the dynamic stall in urban VAWTs at low wind speeds.

The leading-edge protuberance (LEP) represents another promising flow control technology for VAWTs, inspired by the unique design of humpback whale flippers. The effectiveness of LEPs in suppressing flow separation significantly depends on various geometric parameters, including wavelength and wave amplitude. Inadequate geometric parameters can adversely affect the flow performance of a VAWT. Yan *et al.* (2021) discovered that the wave amplitude plays a more critical role than the wavelength in enhancing aerodynamic performance. Furthermore, Chang *et al.* (2024) examined the impact of spacing between protuberances on the performance of biomimetic VAWT blades and reported that blades with long-wavelength LEPs outperform those with short-wavelength counterparts. Consequently, the geometric parameters of LEPs should be thoroughly designed for optimal application on VAWT blades. A crafted blade equipped with leading-edge protuberances can substantially boost the power generation of a VAWT at low tip-speed ratios (TSRs) (Sridhar *et al.*, 2022). Supplementing the already mentioned passive flow control techniques, a range of active control measures are implemented near the leading edge of VAWT blades to reduce flow separation. Rezaeiha *et al.* (2019) implemented leading-edge slot suction to prevent the bursting and formation of laminar separation bubbles, thereby avoiding the development of dynamic stall vortices and trailing-edge roll-up vortices. However, active control technologies necessitate energy consumption, which requires a careful assessment of efficiency and energy expenditure. Abbasi and Daraee (2024) investigated the combined effects of the installation position and actuator activation timing on flow control in a VAWT and proposed a novel method that involves operating plasma actuators for each blade individually to suppress flow separation while minimizing energy consumption.

Trailing-edge control techniques have demonstrated their effectiveness in suppressing flow separation and improving the power coefficient of VAWTs. Among the most commonly employed trailing-edge control methods are trailing-edge jets (Sun & Huang, 2023), Gurney flaps (GFs) (Chen *et al.*, 2020; Zhu *et al.*, 2021; Liu *et al.*, 2022; Syawitri *et al.*, 2024), and trailing-edge flaps (Ertem *et al.*, 2016; Attie *et al.*, 2022; Han *et al.*, 2023). The GF is a small tab attached to the pressure surface of the blade, which increases the blade's chamber. This configuration generates a pair of counter-rotating vortices downstream of the GF, leading to a negative pressure distribution on the suction surface and a positive one on the pressure surface. Zhu *et al.* (2021) conducted a numerical study examining how the geometric parameters of the GF influence the performance of straight-bladed VAWTs. Chen *et al.* (2020) reported that an active GF yields better performance than a fixed GF. Liu *et al.* (2022) explored the combined effects of the GF and cavity on the aerodynamic efficiency of a straight-bladed VAWT. Syawitri *et al.* (2024) proposed a slit-modified GF aimed at reducing drag in lift-type VAWTs. This GF with a slit created small-scale vortices that quickly broke down large coherent flow structures in the near-wake, thus enhancing the lift-to-drag ratio and bettering the torque production. The trailing-edge flap, which is typically separated from the blade by a slot, is more complex than the GF (Ertem *et al.*, 2016). The high-pressure flow that passes through the slot helps delay flow separation and reduces vortex shedding. Attie *et al.* (2022) studied the impact of critical geometric parameters on VAWT performance via the design of experimental methodologies. Furthermore, Han *et al.* (2023) discussed the synergistic control of pitch and trailing-edge flaps in VAWTs, demonstrating that the coordinated motion of pitch and the flap effectively suppress flow separation and minimize load fluctuations in the turbine.

Inspired by the phenomenon where birds slightly increase their feathers at the trailing edge, we propose an adjustable bionic flap (BF) to manage flow separation on the VAWT blade. The configuration of the blade equipped with the BF is depicted in Fig. 1. The BF can significantly mitigate flow separation on a static blade, resulting in an increased lift-to-drag ratio and reduced flow separation (Ma *et al.*, 2022). However, studies focusing on how a BF influences the aerodynamic characteristics of a VAWT are scarce, and the flow dynamics involved with a rotating

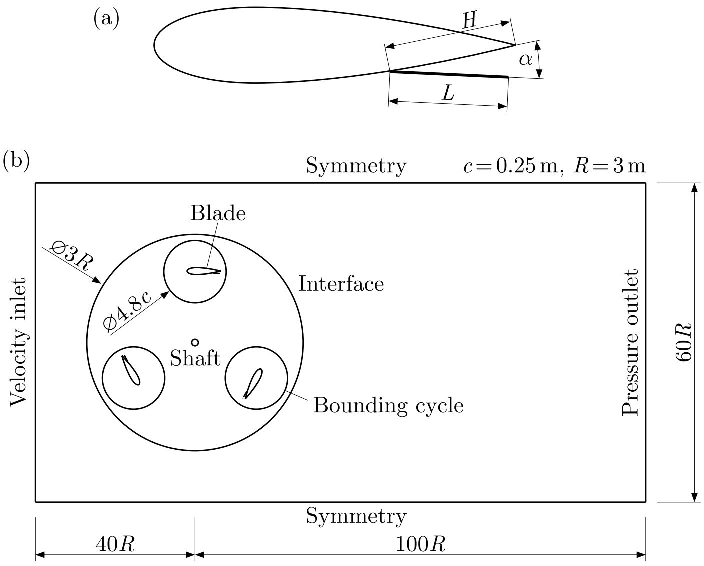

Fig. 1. Geometry models: (a) blade with a BF; (b) computational zone and boundary condition.

VAWT blade equipped with a BF are poorly comprehended. This study utilizes comprehensive numerical simulations conducted with ANSYS Fluent software to explore the flow control mechanisms of the BF on the VAWT blade and evaluate how the geometric parameters of the BF influence the aerodynamic performance of the VAWT. The composition of the paper is set out in the following manner: Section 2 establishes and validates the numerical simulation model; Section 3 discusses the flow control mechanisms of the BF across two typical TSRs; Section 4 investigates the impact of the BF on the power coefficient of the VAWT and the instantaneous torque of a single blade; Section 5 presents the conclusions.

2. Numerical model and validation

2.1. Research subjects

The study focuses on a 12 kW VAWT developed by Uppsala University (Kjellin *et al.*, 2011). This H-type Darrieus wind turbine features a diameter of $R = 3\,\mathrm{m}$ and a height of $H = 5\,\mathrm{m}$. The blade ends are tapered, starting 1 m from the tip, resulting in a chord length at the tip that is 60 % of that at the midpoint of the blade. The blade airfoil is the NACA 0021, and the chord length at the midpoint is $c = 0.25\,\mathrm{m}$. The power coefficient (c_p) as a function of the TSR was measured through field testing at two fixed rotational speeds of 48 and 57. The wind shear and the wind distribution of the test site were measured for several years. The c_p-TSR curve was drawn using around 350 h data from a measurement campaign in 3 months. The wind speed range is 0 m/s–11 m/s, which corresponds to a TSR range of 1.75–4.5. This wind turbine was chosen as such a TSR range covers the main operating range of a VAWT, such as deep dynamic stall and light dynamic stall categories. The primary geometric parameters of the BF are illustrated in Fig. 1. The length between the BF hinge point and the blade trailing edge is denoted as H, the pop-up angle is indicated by α, and the BF length is specified as L. The BF was installed on the inner side of the blade as it performs better than that on the outer side. For convenience, the prototype of the 12 kW VAWT is denoted as the original VAWT, and the VAWT controlled by the BF is denoted as the VAWT with the BF.

2.2. Numerical model

Considering the time-intensive nature of 3D unsteady studies, a 2D unsteady numerical model was constructed on the basis of the blade midsection. The computational domain is depicted in

Fig. 1b. This domain spans $40R$ upstream and $100R$ downstream of the VAWT's centre, having a width of $60R$. A velocity inlet boundary condition is assigned to the upstream boundary. A pressure outlet boundary condition is used for the downstream boundary. A symmetry boundary condition is applied to the top and bottom sides, and a no-slip boundary condition is enforced on the blade surface. The computational domain is partitioned into two regions by a circle that has a diameter of $3R$. The internal subdomain is set up as a rotating zone with a rotation speed of 57 rpm, while the external subdomain is designated as a non-rotating zone. A sliding mesh model is implemented at the interfaces between the two subdomains, utilizing a non-conformal interface. Three bounding cycles are established around the three blades to regulate the grid density, with the diameter of the bounding cycles set at $4.8c$.

As depicted in Fig. 2, a hybrid mesh approach is employed to discretize the computational domain via Gambit 2.4.6. A structured quadrilateral grid is utilized for the external subdomain and the boundary layer of the blade, whereas an unstructured triangular grid is applied to the other regions. The BF disrupts the topology around the blade, requiring a subdomain to be split to include the BF. An unstructured triangular grid is used to discretize this particular subdomain, complemented by 20 layers of quadrilateral grid generated along the BF surface. The height of the first layer along both the blade and BF surfaces is set to 1.2×10^{-5} m, ensuring that the wall y^+ is approximately 1 (Rogowski *et al.*, 2018). The unsteady flows around the VAWTs are analyzed via Fluent 16.1 and the SST k-ω model. The SIMPLE algorithm (Patankar & Spalding, 1972) and a second-order upwind scheme are adopted. The residuals of the unsteady calculations are set 10^{-6}. Thirty revolutions were simulated for each case in the grid independence study. The unsteady flow shows periodicity after the fifteenth revolution. Then, the converged flow field was taken as the initial flow field for the cases with different time steps and TSRs and at least ten more revolutions were performed to obtain periodicity.

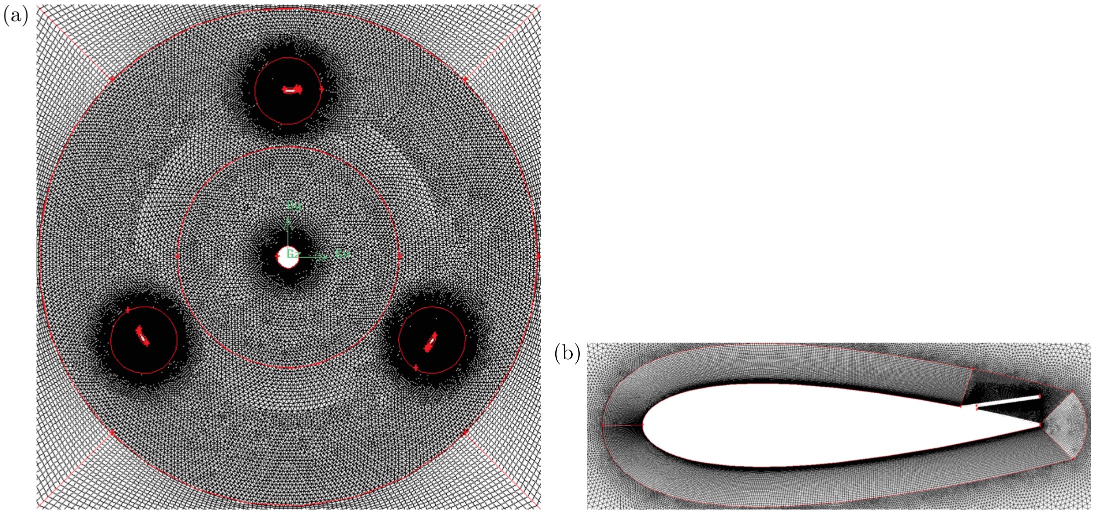

Fig. 2. Grid strategy: (a) grid around the VAWT; (b) gird around the blade with the BF.

The grid independence study was performed on the original VAWT at a TSR of $\lambda = 2.11$, during which the blades undergo deep dynamic stall. The time step was established at $\Delta\theta = 1°$, as the optimal time step is initially unknown. Grid refinement was performed by adjusting the number of cells on the blades, bounding cycles, interfaces, and wakes, as outlined in Table 1. The calculated torques of the VAWT are 54.7, 56.1, 59.6, and 60.7 Nm for the four grid configurations. The relative deviations between Grids 1, 2, 3 and Grid 4 were calculated. The relative deviation decreased with the increase in the grid number. The relative deviation between Grid 3 and Grid 4 dropped to 1.8% and the torque curves of the two grids almost overlapped, as shown in Fig. 3a. Thus, Grid 3 was chosen for the following studies.

Table 1. Grid independence study.

Parameters	Grid 1	Grid 2	Grid 3	Grid 4
Leading-edge spacing [mm]	0.5	0.25	0.1875	0.125
Trailing-edge spacing [mm]	1	0.5	0.375	0.25
Cells on the blade	131	262	370	524
Cells on the bounding cycle	60	180	240	300
Cells on the interfaces	180	360	360	720
Cells on the wake	60	120	180	240
Total number of cells	1.12×10^5	2.73×10^5	3.73×10^5	7.09×10^5
Torque of the VAWT [Nm]	54.7	56.1	59.6	60.7
Relative deviation [%]	−9.88	−7.58	−1.81	–

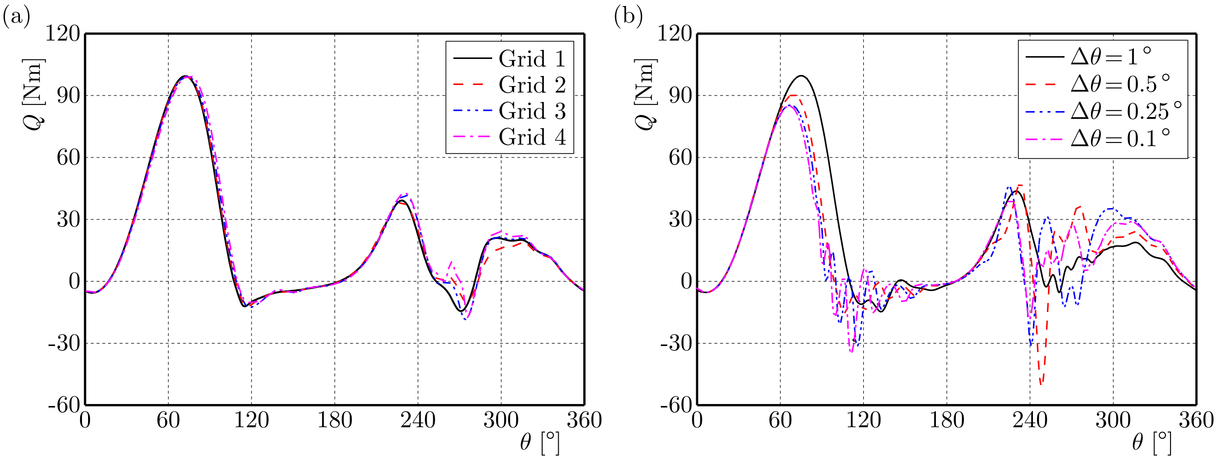

Fig. 3. Results of grid and time independence studies:
(a) grid independence study; (b) time independence study.

A time independence study was conducted on Grid 3 at $\lambda = 2.11$. Four time steps were considered: $\Delta\theta = 1°$, $0.5°$, $0.25°$, and $0.1°$. The torque of a single blade versus the azimuthal angle, θ, is compared in Fig. 3. The torque curve appears relatively smooth when $\Delta\theta = 1°$. This time step is not sufficiently small to capture the fluctuations in torque caused by the shedding of the dynamic stall vortex (Rezaeiha *et al.*, 2018). When the time step is reduced to $\Delta\theta = 0.25°$, fluctuations in the torque are accurately captured. The torque curve subsequently exhibits minimal change as the time step decreases further. The torques of the VAWT at the four time steps are 59.6, 50.7, 48.1, and 48.0 Nm, respectively. Therefore, a time step of $\Delta\theta = 0.25°$ was selected for simulating the flow around the VAWT.

2.3. Model accuracy evaluation

The numerical model was validated by comparing the predicted power coefficient against the experimental ones from Uppsala University (Kjellin *et al.*, 2011), as depicted in Fig. 4. The results are in close agreement with the experiment data at low TSRs. However, a deviation is noted at high TSRs, which is consistent with findings in other studies (Daróczy *et al.*, 2015). These deviations primarily stem from two factors: first, the numerical error brought by discretization schemes, which is inevitable in the process of converting partial differential equations into linear equations; second, the adoption of a 2D numerical simulation, which overlooks losses induced by 3D effects, such as blade tip loss and support arm loss. These 3D losses tend to increase with increasing TSR. Daróczy *et al.* (2015) proposed a correction for these deviations represented by $\Delta C_p^{\mathrm{corr}} = -0.0021\lambda^3$. As shown in Fig. 4, the modified values correspond closely with the

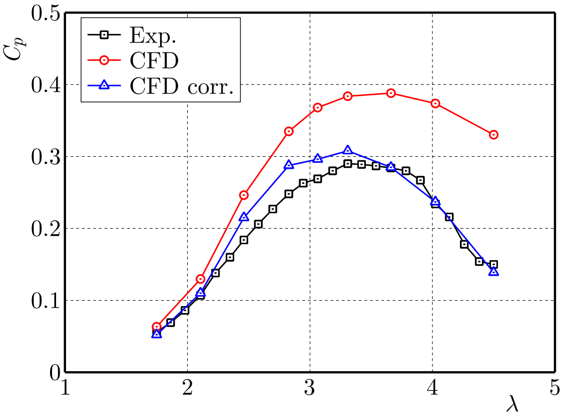

Fig. 4. Validation of the numerical model by power coefficient.

experiment data. The aim of this research is to explore the mechanism of the BF in the flow separation. The influence of the BF on the three-dimensional effects is considered relatively minor and is thus excluded from further discussion. Consequently, the numerical model is deemed sufficiently accurate for the current investigation.

3. Flow control mechanism of the BF

Due to the drag induced by the BF, not well-deigned BF may lead to a deterioration of the VAWT power coefficient for $\lambda > 3.66$. The BF with $L20H20\alpha15$ is chosen to analyze its effect on flow separation, as the case presents a positive effect on the power coefficient of the VAWT from $\lambda = 1.75$ to $\lambda = 3.66$. This TSR range covers the deep and light dynamic stall categories of a VAWT. The case of $L20H20\alpha15$ denotes $L = 0.2c$, $H = 0.2c$, and $\alpha = 15°$.

3.1. $\lambda = 1.75$

Figure 5 illustrates the impact of the BF on the torque of a single blade over one rotation period at $\lambda = 1.75$. The blades experience significant dynamic stall due to a dramatic change in the local angle of attack (AoA). Evident changes can be observed within the range of $\theta = 0°$ to 100° in the upwind position and $\theta = 270°$ to 360° in the downwind position. The average torque of the blade with the BF increases by 35.8 %, with the average torque increasing by 5.1 % in the upwind position and 87.8 % in the downwind position.

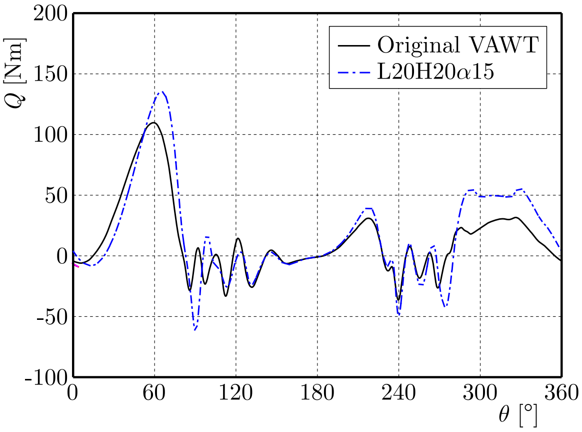

Fig. 5. Torque of a single blade vs. azimuthal angle for $\lambda = 1.75$.

In the upwind position, the torque of the blade with the BF slightly decreases within the range of $\theta = 8°$ to 52°, where the theoretical local AoA varies from 2.9° to 19.4°. During this phase, the blade encounters a light dynamic stall, characterized by mostly attached flow or mild flow separation. The presence of the BF restricts the acceleration of flow at the blade's leading edge, resulting in a reduction in lift. With the increase in the azimuthal angle, the local AoA keeps increasing. The torque of the original blade stalls at $\theta = 60°$. As indicated in Fig. 6a, the separation point shifts toward the middle of the blade surface, forming a pair of counter-rotating vortices at the trailing edge. The BF aids in delaying the stall phenomenon. Notably, the torque of the blade with the BF exceeds that of the original blade at $\theta = 52°$ and begins to decrease at $\theta = 66°$. Figure 6b shows that the BF hinders the development of the anticlockwise rotating vortex, resulting in a significantly smaller vortex than that of the original blade, ultimately accelerating the flow at the leading edge. Consequently, the region of negative pressure expands, and its magnitude increases, accounting for the increase in torque from $\theta = 52°$ to 86°. However, after this range, the blade enters a state of deep stall, rendering the BF ineffective.

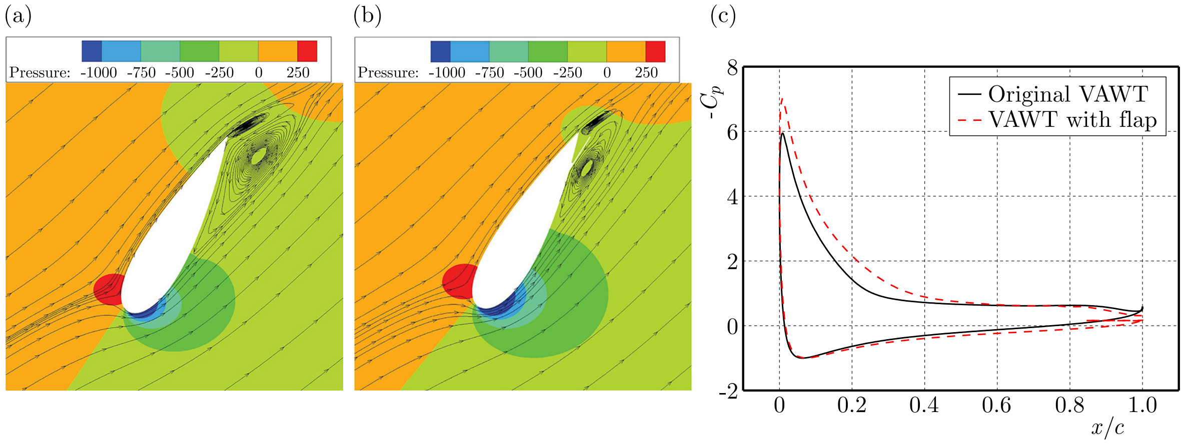

Fig. 6. Flow fields and pressure distributions around the blades at $\theta = 66°$: (a) original blade; (b) blade with the BF; (c) pressure distribution.

In the downwind position, the BF significantly enhances the torque during the rotational period. A notable increase in torque is observed within the range of $\theta = 282°$ to 360°, where the local AoA gradually decreases. As depicted in Fig. 7, the flow reattaches to the blade surface as the azimuthal angle progresses. The BF functions similarly to a GF, improving blade torque through two key mechanisms. First, the BF significantly reshapes the flow field at the trailing edge of the blade. The vortex core at the trailing edge of the blade with the BF is displaced downstream, enhancing the camber effect. This alteration hastens the flow velocity at the leading edge, thereby increasing the negative pressure on the outer surface of the blade with the BF. Second, flow over the inner surface of the blade with the BF experiences blockage and deceleration, due to the changed core position of the trailing-edge vortex and the raised height of the BF. Consequently, the pressure on the inner surface of the blade with the BF goes up. The combined effects of these two mechanisms lead to an increased pressure differential between the inner and outer surfaces of the blade, ultimately enhancing the lift generated by the blade with the BF.

3.2. $\lambda = 3.31$

Figure 8 illustrates the impact of the BF on the torque of a single blade during a rotation period at $\lambda = 3.31$. The blades exhibit light dynamic stall. The torque fluctuations depicted in Fig. 8 are noticeably reduced compared with those observed at $\lambda = 1.75$. The blade with the BF demonstrated an average torque increment of 7.7 % as opposed to the original blade. However, the average torque of the blade with the BF drops by 16.0 % when in the upwind position. This decline in torque is primarily evident within the range of $\theta = 15°$ to 103°. The theoretical local

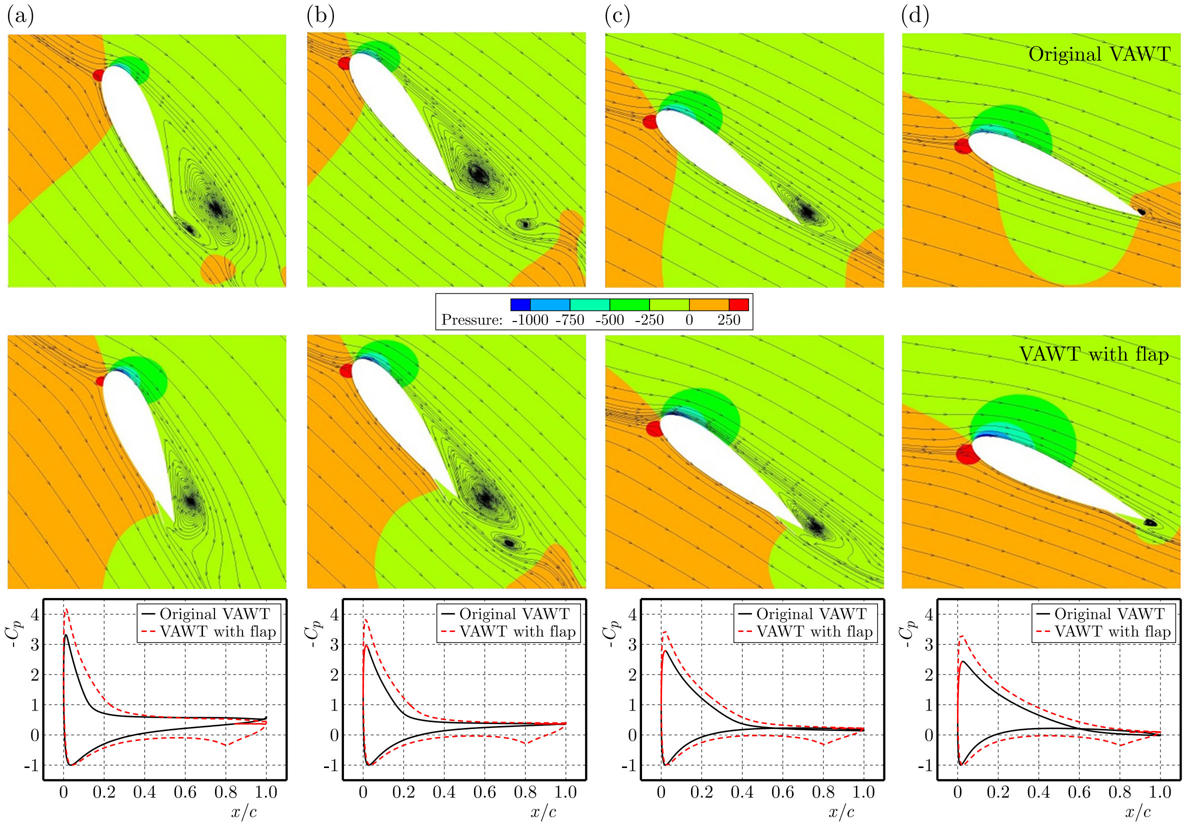

Fig. 7. Flow fields and pressure distributions around the blades at:
(a) $\theta = 288°$, (b) $\theta = 300°$, (c) $\theta = 315°$, (d) $\theta = 330°$.

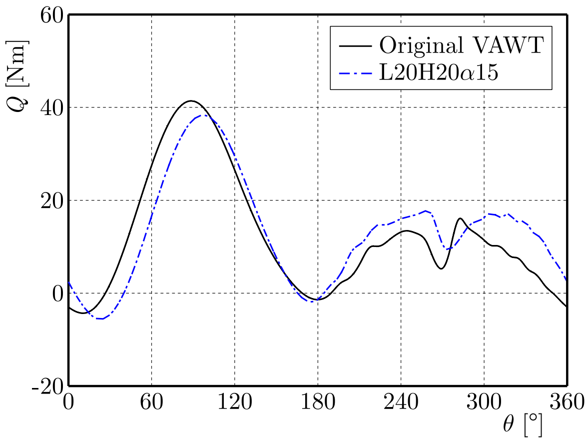

Fig. 8. Torque of a single blade vs. azimuthal angle for $\lambda = 3.31$.

AoA falls between 3.5° and 17.5°. The reasoning behind this phenomenon aligns with that at $\lambda = 1.75$.

The increase in torque for the blade with the BF is attributed entirely to the downwind position, where the average torque increases by 60.4 % as compared to the original blade. Flow attachment is consistently maintained in the downwind positions. As demonstrated in Fig. 9, the BF redirects the flow near the trailing edge, altering the Kutta condition and enhancing the flow circulation around the blade. Furthermore, a pair of counter-rotating vortices forms on the inner surface of the trailing edge of the blade with the BF. The shedding of these vortices increases the suction force on the outer surface of the blade while increasing the pressure on the inner surface by decelerating the flow.

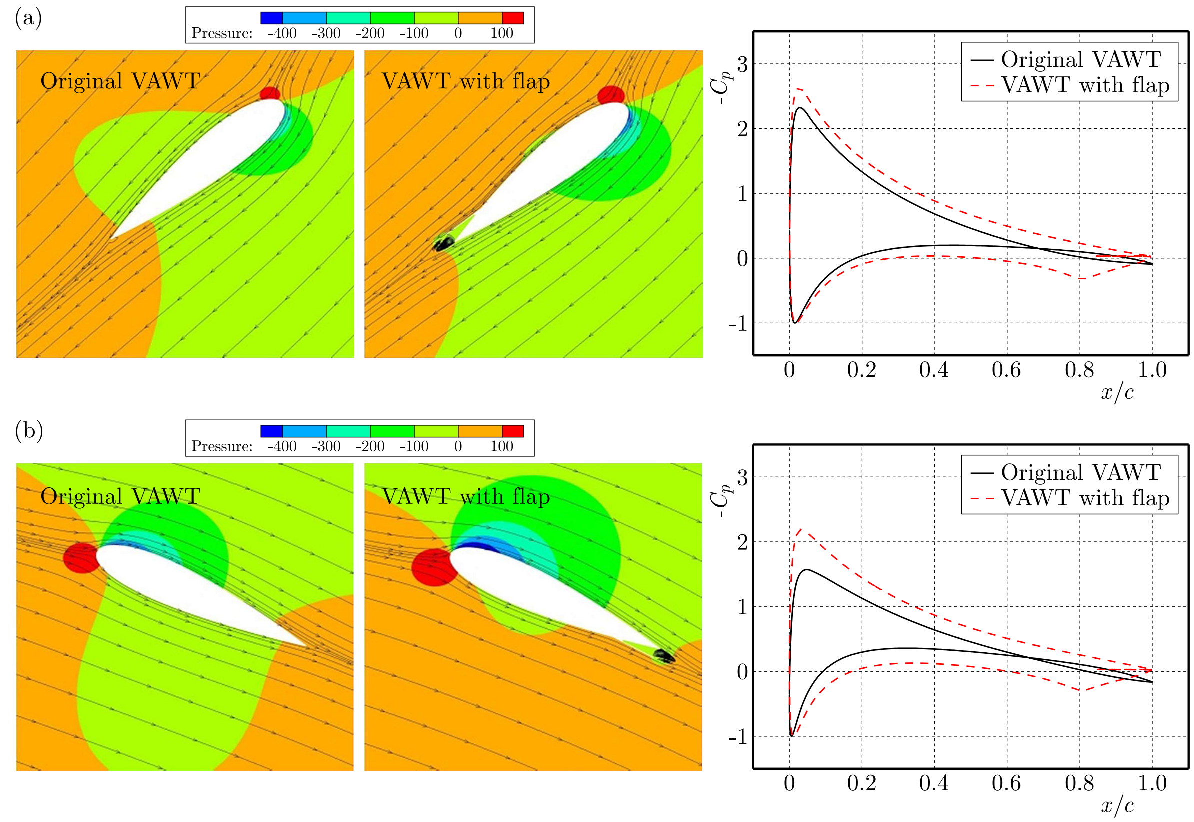

Fig. 9. Flow fields and pressure distributions around the blades at: (a) $\theta = 225°$; (b) $\theta = 330°$.

4. Effects of the BF geometry parameters

The primary geometrical parameters of the BF, as illustrated in Fig. 1, significantly influence the aerodynamic performance of the VAWT. This section discusses the effects of these parameters on the power coefficient of the VAWT and the torque of a single blade.

4.1. Pop-up angle of the BF

A contrast of the power coefficients of the original VAWT and the VAWT with the BF at varying pop-up angles (α) is depicted in Fig. 10. The parameters L and H are both fixed at $0.2c$. The power coefficients are significantly enhanced by the adding of the BF when the TSR $\lambda \leq 3.06$. A relatively large pop-up angle is beneficial for improving the power coefficient

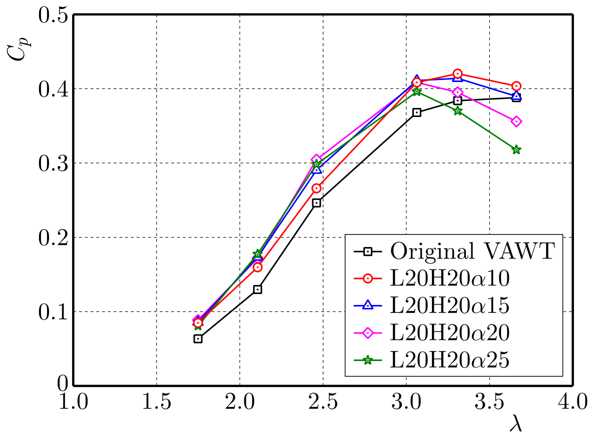

Fig. 10. Power coefficient as a function of TSR at different pop-up angles.

at lower TSRs ($\lambda < 3.06$), with a maximum relative increment of 39.6 % observed at $\lambda = 1.75$ for $\alpha = 20°$.

Figure 11a presents the torques of a single blade as a function of the azimuthal angle for different pop-up angles at $\lambda = 1.75$. Notably, a greater pop-up angle hinders the acceleration of the flow along the inner surface of the blade within the range of $\theta = 8°$ to 60°. The case with $\alpha = 25°$ results in the most significant decrease in torque. However, in the range of $\theta = 60°$ to 86°, a larger pop-up angle delivers superior performance, as the BF efficiently suppresses the trailing-edge vortex. In the downwind position, the relative increments in the average torque of the blade with the BF as compared to the original blade are 76.5 %, 87.8 %, 107.1 %, and 103.7 %, respectively.

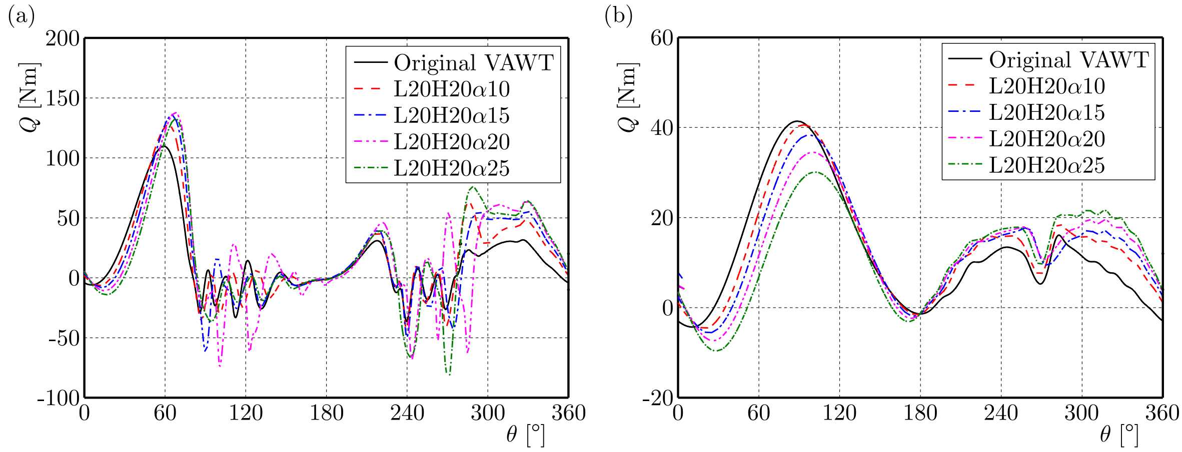

Fig. 11. Torque of a single blade vs. azimuthal angle for different pop-up angles:(a) $\lambda = 1.75$; (b) $\lambda = 3.31$.

As depicted in Fig. 12, the variations in pressure distribution among these cases at $\lambda = 1.75$ are primarily concentrated on the leading edge of the blade's outer surface and the trailing edge of the blade's inner surface. A larger pop-up angle promotes the flow speedup near the leading edge on the outer surface and slows down the flow near the trailing edge on the inner surface. Thus, the negative pressure at the leading edge and the positive pressure at the trailing edge rise as the pop-up angle enlarges. However, a relatively large pop-up angle also induces additional fluctuations in torque, which can negatively affect the fatigue life of the blade.

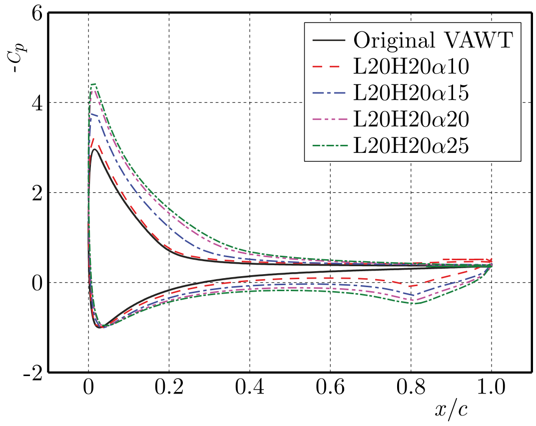

Fig. 12. Pressure distributions around the blades at $\theta = 300°$ for different pop-up angles.

In contrast, a relatively small pop-up angle is beneficial for enhancing the power coefficient at a TSR of $\lambda \geq 3.06$. Specifically, the case with an angle of $\alpha = 10°$ has the highest power coefficient within the range of $\lambda = 3.06$ to 3.66. Compared with those of the original VAWT, the relative increases in the power coefficient are 11.0 %, 9.5 %, and 4.0 % for λ values of 3.06, 3.31, and 3.66, respectively. Notably, the relative increment in the power coefficient diminishes as the pop-up angle increases. However, for a pop-up angle of $\alpha = 25^\circ$, the power coefficient of the VAWT with a BF becomes lower than that of the original VAWT at $\lambda = 3.31$, with a further reduction observed at $\lambda = 3.66$. Compared with the original VAWT, the relative decrements in the power coefficient at $\lambda = 3.66$ are 8.3 % and 18.1 % for the cases with $\alpha = 20^\circ$ and $\alpha = 25^\circ$, respectively.

Figure 11b shows the torques of a single blade versus the azimuthal angle for various pop-up angles at $\lambda = 3.31$. The torque of the VAWT with the BF clearly decreases as the pop-up angle increases in the upwind position. Conversely, the opposite trend is observed in the downwind direction. However, the improvement in torque during the downwind position does not mitigate the reduction experienced in the upwind position for the case with $\alpha = 25^\circ$. Consequently, a relatively small pop-up angle is recommended for enhancing the power coefficient of a VAWT with a BF at a wider TSR range.

For an adjustable BF, the pop-up angle can be tailored on the basis of either the TSR or the azimuthal angle. By tuning the pop-up angle in accordance with the TSR, the power coefficient of the VAWT with an adjustable BF can be determined by selecting the maximum value at each TSR, as shown in Fig. 10. If the pop-up angle is modified on the basis of the azimuthal angle, the BF remains retracted at the azimuthal angles where the flap negatively affects the torque. Two optimal control strategies are formulated on the basis of the findings in Fig. 11 for $\lambda = 1.75$ and 3.31. As depicted in Fig. 13, the BF remains retracted within the range of $\theta = 0^\circ$ to 53° while extending to a pop-up angle of 15° in the range of $\theta = 53^\circ$ to 360° at $\lambda = 1.75$. Compared with the original VAWT, the power coefficient of the VAWT with the BF is enhanced by 45.2 %, which is 5.6 % greater than that of the $L20H20\alpha20$ configuration. For $\lambda = 3.31$, the BF remains retracted in the upwind position while extending to a pop-up angle of 25° in the downwind position. Compared with that of the original VAWT, the power coefficient of the VAWT with the BF increases by 28.9 %, which is 19.4 % greater than that of the $L20H20\alpha10$ configuration. Thus, the adjustable BF demonstrates superior performance in improving the power coefficient relative to a fixed BF. However, the above inference was based on the results of the BF with a fixed pop-up angle. An adjustable BF may influence the development of the vortices and the pressure distribution, which affects the torque history and the power coefficient. Further studies are warranted to reveal the effect of an adjustable BF on the flow separation of the VAWT blade.

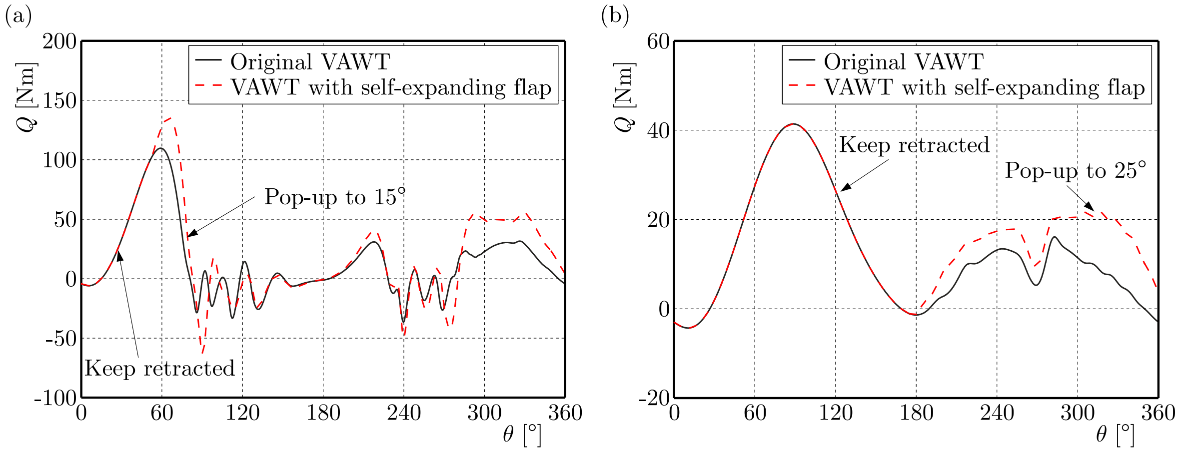

Fig. 13. Torque of a single blade for the VAWT with an adjustable BF: (a) $\lambda = 1.75$; (b) $\lambda = 3.31$.

4.2. Length of the BF

Figure 14 shows the relationship between the length of the BF and the power coefficient, with parameters H and α holding constant at $H = 0.2c$ and $\alpha = 20^\circ$. The variations in the power coefficient caused by changes in BF length are analogous to those induced by alterations in the

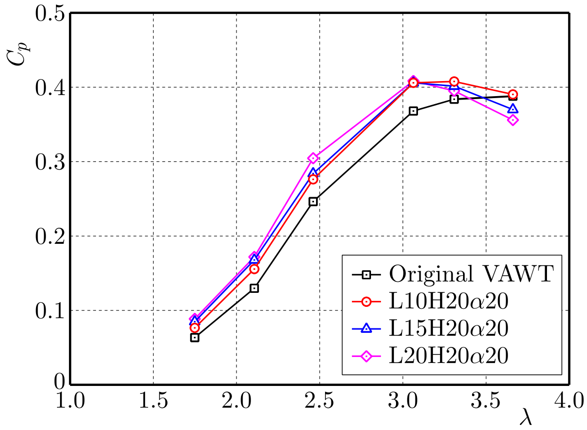

Fig. 14. Power coefficient as a function of TSR at different lengths.

pop-up angle. For $\lambda < 3.06$, the VAWT with a longer BF results in a higher power coefficient. For $\lambda \geq 3.06$, the BF with $L = 0.1c$ outperforms the other two configurations.

4.3. Hinge position of the BF

The hinge position of the BF significantly influences the power coefficient of the VAWT and the torque of a single blade. As shown in Fig. 15, parameters L and α remain constant at $L = 0.2c$ and $\alpha = 20°$. The introduction of the BF leads to substantial increases in power coefficients for $\lambda \leq 3.06$, with a maximum relative increment of 41.3 % observed at $\lambda = 2.11$ with $H = 0.3c$. No discernible trends emerge regarding the effect of the hinge position on the power coefficient of the VAWT with the BF for $\lambda < 3.06$. However, the flap with $H = 0.25c$ demonstrates a smaller improvement in the power coefficient than the other two configurations do. At $\lambda \geq 3.06$, shifting the hinge point of the BF to the blade's leading edge culminates in a diminished power coefficient. The most significant relative reduction is 23.3 % at $\lambda = 3.66$ for $H = 0.3c$.

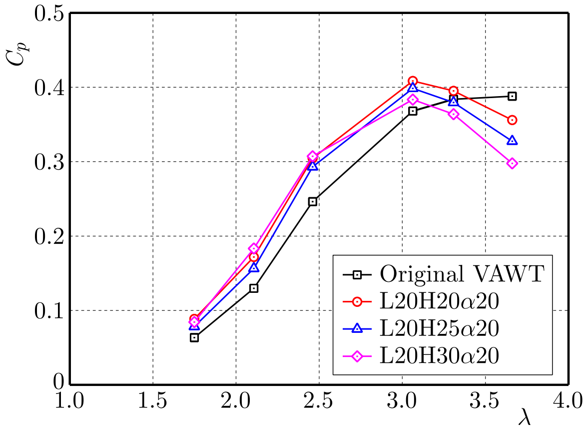

Fig. 15. Power coefficient as a function of TSR at different hinge positions.

5. Conclusions

Numerical simulations are conducted to elucidate the mechanisms by which the BF alleviates flow separation in the VAWT blade and its resultant effects on the power coefficient of the VAWT. The conclusions are as follows:

1) Different mechanisms are exhibited by the BF on blade flow control for the upwind and downwind positions. A BF attached to the inner surface of the blade impedes the development of the trailing-edge vortex at large AoAs when the blade is operating in the upwind

position. Compared with the original blade, the dimensions of the trailing-edge vortex are substantially diminished, which enhances the flow speedup at the leading edge of the blade with a BF. However, the BF impedes flow acceleration at the leading edge at low AoA and detracts from the blade torque at high TSRs. In contrast, when the blade operates in the downwind position, the BF functions similarly to a GF and contributes most to the torque increment, making the BF advantageous for improving torque in the VAWT across a broad range of TSRs.

2) The BF positioned on the inner surface of the blade significantly enhances the power coefficient when $\lambda \leq 3.06$. As the TSR increases further, its effect on power coefficient improvement diminishes due to the decrease in the local AoA. Additionally, the influence of the BF on the power coefficient is contingent upon the three geometric parameters. According to the parameter study, it is recommended to install the BF near the trailing edge of the blade, a hinge position $H < 0.2c$ and the pop-up angle should be smaller than 15°. A multi-objective optimization is needed for improving the power coefficient for a wider range of TSR.
3) Compared with a fixed BF, an adjustable BF, tailored on the basis of the azimuthal angle, has greater potential for improving the power coefficient. Compared with those of the original VAWT, the power coefficients of the VAWT with an adjustable BF are elevated by 45.2 % at $\lambda = 1.75$ and by 28.9 % at $\lambda = 3.31$, significantly outpacing the performance of the VAWT with a fixed BF. Further in-depth studies are necessary to develop a control strategy for the pop-up action of the flap.

Acknowledgments

The Natural Science Foundation of Jiangxi Province (grant no. 20224BAB214061 and 20242BAB20217), the National Natural Science Foundation of China (grant no. 52166002).

References

1. Abbasi, S., & Daraee, M.A. (2024). Ameliorating a vertical axis wind turbine performance utilizing a time-varying force plasma actuator. *Scientific Reports*, *14*, Article 18425. https://doi.org/10.1038/s41598-024-69455-8

2. Abdolahifar, A., & Zanj, A. (2025). A review of available solutions for enhancing aerodynamic performance in Darrieus vertical-axis wind turbines: A comparative discussion. *Energy Conversion and Management*, *327*, Article 119575. https://doi.org/10.1016/j.enconman.2025.119575

3. Attie, C., ElCheikh, A., Nader, J., & Elkhoury, M. (2022). Performance enhancement of a vertical axis wind turbine using a slotted deflective flap at the trailing edge. *Energy Conversion and Management*, *273*, Article 116388. https://doi.org/10.1016/j.enconman.2022.116388

4. Chang, H., Li, D., Zhang, R., Wang, H., He, Y., Zuo, Z., & Liu, S. (2024). Effect of discontinuous biomimetic leading-edge protuberances on the performance of vertical axis wind turbines. *Applied Energy*, *364*, Article 123117. https://doi.org/10.1016/j.apenergy.2024.123117

5. Chen, L., Xu, J., Dai, R. (2020). Numerical prediction of switching gurney flap effects on straight bladed VAWT power performance. *Journal of Mechanical Science and Technology*, *34*(12), 4933–4940. https://doi.org/10.1007/s12206-020-2106-z

6. Daróczy, L., Janiga, G., Petrasch, K., Webner, M., & Thévenin, D. (2015). Comparative analysis of turbulence models for the aerodynamic simulation of H-Darrieus rotors. *Energy*, *90*(Part 1), 680–690. https://doi.org/10.1016/j.energy.2015.07.102

7. Ertem, S., Ferreira, C.S., Gaunaa, M., & Madsen, H.A. (2016). Aerodynamic optimization of vertical axis wind turbine with trailing edge flaps. *34th Wind Energy Symposium, AIAA 2016-1735.* https://doi.org/10.2514/6.2016-1735

8. Han, Z., Chen, H., Chen, Y., Su, J., Zhou, D., Zhu, H., Xia, T., & Tu, J. (2023). Aerodynamic performance optimization of vertical axis wind turbine with straight blades based on synergic control of pitch and flap. *Sustainable Energy Technologies and Assessments*, *57*, Article 103250. https://doi.org/10.1016/j.seta.2023.103250

9. Kjellin, J., Bülow, F., Eriksson, S., Deglaire, P., Leijon, M., & Bernhoff, H. (2011). Power coefficient measurement on a 12 kW straight bladed vertical axis wind turbine. *Renewable Energy*, *36*(11), 3050–3053. https://doi.org/10.1016/j.renene.2011.03.031

10. Liu, Q., Miao, W., Ye, Q., & Li, C. (2022). Performance assessment of an innovative Gurney flap for straight-bladed vertical axis wind turbine. *Renewable Energy*, *185*, 1124–1138. https://doi.org/10.1016/j.renene.2021.12.098

11. Ma, Q., Wang, J., Zhang, Y., Ma, L., Lin, J., & Liu, X. (2022). Research on optimized design of structural parameters and aerodynamics of wind turbine airfoil with bionic flap (in Chinese). *Journal of Xi'an Jiaotong University*, *56*(11), 31–40.

12. McKenna, R., Lilliestam, J., Heinrichs, H.U., Weinand, J., Schmidt, J., Staffell, I., Hahmann, A.N., Burgherr, P., Burdack, A., Bucha, M., Chen, R., Klingler, M., Lehmann, P., Lowitzsch, J., Novo, R., Price, J., Sacchi, R., Scherhaufer, P., Schöll, E.M., Visconti, P., Camargo, L.R. (2025). System impacts of wind energy developments: Key research challenges and opportunities. *Joule*, *9*(1), Article 101799. https://doi.org/10.1016/j.joule.2024.11.016

13. Patankar, S.V., & Spalding, D.B. (1972). A calculation procedure for heat, mass and momentum transfer in three-dimensional parabolic flows. *International Journal of Heat and Mass Transfer*, *15*(10), 1787–1806. https://doi.org/10.1016/0017-9310(72)90054-3

14. Syawitri, T.P., Yao, Y., Yao, J., & Chandra, B. (2024). Drag reduction of lift-type Vertical axis wind turbine with slit modified Gurney flap. *Journal of Wind Engineering and Industrial Aerodynamics*, *253*, Article 105853. https://doi.org/10.1016/j.jweia.2024.105853

15. Rehman, S., Alhems, L.M., Alam, M.M., Wang, L., & Toor, Z. (2023). A review of energy extraction from wind and ocean: Technologies, merits, efficiencies, and cost. *Ocean Engineering*, *267*, Article 113192. https://doi.org/10.1016/j.oceaneng.2022.113192

16. Rezaeiha, A., Montazeri, H., & Blocken, B. (2018). Towards accurate CFD simulations of vertical axis wind turbines at different tip speed ratios and solidities: Guidelines for azimuthal increment, domain size and convergence. *Energy Conversion and Management*, *156*, 301–316. https://doi.org/10.1016/j.enconman.2017.11.026

17. Rezaeiha, A., Montazeri, H., & Blocken, B. (2019). Active flow control for power enhancement of vertical axis wind turbines: Leading-edge slot suction. *Energy*, *189*, Article 116131. https://doi.org/10.1016/j.energy.2019.116131

18. Rogowski, K., Hansen, M.O.L., & Maronski, R. (2018). Steady and unsteady analysis of NACA 0018 airfoil in vertical-axis wind turbine. *Journal of Theoretical and Applied Mechanics*, *56*(1), 203–212. https://doi.org/10.15632/jtam-pl.56.1.203

19. Sridhar, S., Joseph, J., & Radhakrishnan, J. (2022). Implementation of tubercles on Vertical Axis Wind Turbines (VAWTs): An aerodynamic perspective. *Sustainable Energy Technologies and Assessments*, *52*(Part B), Article 102109. https://doi.org/10.1016/j.seta.2022.102109

20. Sun, J., & Huang, D. (2023). Impact of trailing edge jet on the performance of a vertical axis wind turbine. *Journal of Mechanical Science and Technology*, *37*(3), 1301–1309. https://doi.org/10.1007/s12206-023-0216-0

21. Tayebi, A., & Torabi, F. (2024). Flow control techniques to improve the aerodynamic performance of Darrieus vertical axis wind turbines: A critical review. *Journal of Wind Engineering and Industrial Aerodynamics*, *252*, Article 105820. https://doi.org/10.1016/j.jweia.2024.105820

22. Ullah, T., Javed, A., Abdullah, A., Ali, M., & Uddin, E. (2020). Computational evaluation of an optimum leading-edge slat deflection angle for dynamic stall control in a novel urban-scale vertical axis wind turbine for low wind speed operation. *Sustainable Energy Technologies and Assessments*, *40*, Article 100748. https://doi.org/10.1016/j.seta.2020.100748

23. Yan, Y., Avital, E.J., Williams, J., & Cui, J. (2019). CFD analysis for the performance of micro-vortex generator on aerofoil and vertical axis turbine. *Journal of Renewable and Sustainable Energy*, *11*(4), Article 043302. https://doi.org/10.1063/1.5110422

24. Yan, Y., Avital, E.J., Williams, J., & Cui, J. (2021). Aerodynamic performance improvements of a vertical axis wind turbine by leading-edge protuberance. *Journal of Wind Engineering and Industrial Aerodynamics*, *211*, Article 104535. https://doi.org/10.1016/j.jweia.2021.104535

25. Zhao, Z., Wang, D., Wang, T., Shen, W., Liu, H., & Chen, M. (2022). A review: Approaches for aerodynamic performance improvement of lift-type vertical axis wind turbine. *Sustainable Energy Technologies and Assessments*, *49*, Article 101789. https://doi.org/10.1016/j.seta.2021.101789

26. Zhong, J., Li, J., Guo, P., & Wang, Y. (2019). Dynamic stall control on a vertical axis wind turbine aerofoil using leading-edge rod. *Energy*, *174*, 246–260. https://doi.org/10.1016/j.energy.2019.02.176

27. Zhu, H., Hao, W., Li, C., Luo, S., Liu, Q., & Gao, C. (2021). Effect of geometric parameters of Gurney flap on performance enhancement of straight-bladed vertical axis wind turbine. *Renewable Energy*, *165*(Part 1), 464–480. https://doi.org/10.1016/j.renene.2020.11.027

Manuscript received December 3, 2024; accepted for publication April 3, 2025;